Archive of Applied Mechanics (2021) 91:545–562
https://doi.org/10.1007/s00419-020-01836-7

ORIGINAL

Sonja Uebing · Dominik Brands · Lisa Scheunemann · Jörg Schröder

Residual stresses in hot bulk formed parts: two-scale approach for austenite-to-martensite phase transformation

Received: 29 May 2020 / Accepted: 29 October 2020 / Published online: 11 January 2021

Abstract In production engineering, current research focuses on the induction of targeted residual stress states in components in order to improve their properties. Therein, the combination of experiment and simulation plays an important role. In this contribution, a focus is laid on the investigation of hot forming processes with subsequent cooling. A numerical approach is presented to analyze the distribution of residual stresses resulting from cooling of a cylinder with an eccentric hole made of chromium-alloyed steel. The occurring phase transformation, which is evoked by cooling, is considered in order to compute residual stress distributions inside the material.

Keywords Residual stresses · Multiscale computation · Austenite–martensite phase transformation · Cr-alloyed steel · Hot bulk forming · Cooling

1 Introduction

In the last decades, the experimental and numerical analysis of residual stresses has gained importance in the field of material science. In course of that, compressive residual stresses in regions close to the surface seem to lead to superior behavior compared to tensile residual stresses. The idea of generating a specific residual stress state to improve the final component's properties, e.g., geometry, strength or durability, has become a focus today. Therefore, in McMeeking and Lee [23], Tekkaya et al. [45], Bonn [6], Mungi et al. [30], Fei and Hodgson [7], Moen et al. [27], and Ma et al. [20] the relation of forming conditions and final residual stress distributions is examined. In particular, hot forming processes offer the opportunity to adjust certain process parameters, such as deformation state or temperature profile by manipulating parameters such as cooling or deformation rate in order to induce targeted residual stress states.

Following Macherauch et al. [21], residual stresses are characterized by the scale they act on. A distinction is made between residual stresses of first type which are the average over residual stresses in a certain macroscopic section of the component (averaged over several grains) and residual stresses of second and third type which refer to the average over a grain, as deviation of the residual stress amplitudes of the first type, and within a grain, respectively. Thus, residual stresses of first type are also called macroscopic residual stresses and strongly influence the final macroscopic component's properties. Residual stresses of second and third type are often called microscopic which of course influence residual stresses of first type.

Residual stresses can be caused by various phenomena, e.g., thermal, mechanical or chemical effects. This work focuses on residual stresses mainly influenced by microscopic phase transformation which is evoked by subsequent cooling after a hot forming process. For the description of considered austenite-to-martensite

S. Uebing (✉) · D. Brands · Lisa Scheunemann · J. Schröder
Abtl. Bauwissenschaften, Fakultät für Ingenieurwissenschaften, Institut für Mechanik, Universität Duisburg-Essen, Universitätsstr. 15, 45141 Essen, Germany
E-mail: sonja.uebing@uni-due.de

phase transformation, Bain groups can be applied, see, e.g., Bhattacharya [5]. The fundamental work in the field of Bain groups has been done in Bain and Dunkirk [1], Bain and Griffiths [2]. They take into account three different variants of martensite, resulting from lattice shearing of austenitic face-centered cubic unit cells to martensitic body-centered tetragonal transformed unit cells. Such three martensitic variants are related to a volume expansion compared to the austenitic unit cell, see Moyer and Ansell [28].

The research on solid–solid phase transformation has been an active field of research for several decades, where the phase transformation kinetics in terms of volume fractions have been discussed in, for example, Levitas et al. [18], Stringfellow et al. [44] and Simonsson [42], among others. The first approaches using a thermomechanical description have been done by, e.g., Ganghoffer et al. [9] and Levitas [11–14]. The theory of general phase transformation is explained for example in Levitas [15,16], Levitas et al. [19] and extended to martensite in particular in Levitas [17]. Experimental work in this field can be found, e.g., in Park [34]. In course of that, an overview on the derivation of the continuum mechanical formulation is given in Fischer et al. [8], while Roters et al. [35] addresses a crystal plasticity finite element model for the computation of phase transformation. More recent works regarding solid–solid phase transformation and its numerical description are, for example, Mahnken et al. [22] where a phenomenological approach has been proposed based on an additive strain decomposition in the regime of small strains. In Behrens et al. [3], the authors focus on the verification of numerical simulation using experiments. In recent decades, the phase-field modeling has become an alternative computational approach to model transformation processes, see, e.g., Schneider et al. [36,37], Schoff et al. [38]. In the work of Müller [29], the austenite-to-martensite phase transformation is illustrated based on Olson and Cohen [32,33], in which the fundamental characteristics of the atomic lattice and its transition are explained.

In this contribution, an approach for the numerical analysis of the residual stress state of a cooled cylinder with an eccentric hole is presented wherein the occurring phase transformation is handled using a phenomenological approach. The experimental procedure is described in detail in Simsir and Gür [43]. Motivated by the definition of residual stresses on multiple scales, a multiscale approach is proposed which enables the analysis of different physical phenomena. Here, the focus lies on the effects due to the austenite-to-martensite phase transformation. Section 2 gives a short overview of the process and most important material and process data. In Sect. 3, a two-scale finite element simulation and a model to consider the phase transformation are described. Additionally, temperature dependent material parameters used to simulate the cooling process are calibrated. The calibration is done by relating the simulated curves to material data, which is provided from the Institute of Forming Technology and Machines, Leibniz University Hannover, e.g., Behrens et al. [4]. For the proposed model, studies regarding the finite element discretization as well as the time step size are presented in Sect. 4. The final discretization and time step size are used to explore the residual stress evolution during the total cooling process. A conclusion of the paper is given in Sect. 5.

2 Experimental setup

The considered specimen is a cylinder with an eccentric hole made of chromium-alloyed steel 1.3505 (100Cr6), see Fig. 1. The eccentricity e, cf. Fig. 1b, of the hole is chosen in order to evoke inhomogeneous stress distributions, see Simsir and Gür [43].

In the beginning of the hot forming process, the material is heated to over 1000 °C, such that it is fully austenized. Together with a suitable soaking time, an initial state is achieved with a relaxed inner stress state. From an atomistic point of view, austenite is characterized by face-centered cubic (fcc) unit cells. After the upsetting, which reduces the height by approximately 50%, the specimen is cooled in water. This rapid cooling below the martensitic start temperature θ_{Ms} triggers a diffusionless phase transformation to martensite, which is defined by a lattice transformation to body-centered tetragonal (bct). The rearrangement of the atomic lattice results in a volume expansion when comparing the fcc and bct lattice, see Moyer and Ansell [28]. Here, a volume expansion of 2% is taken into account based on Olle [31]. Figure 2 illustrates the cooling route and phase transformation.

The cooling process covers a time range of 80 s. Data regarding the time–temperature relation on the lateral surface and the temperature–volume fraction relation are provided by simulations of the Institute of Forming Technology and Machines (IFUM), Leibniz University Hannover. In Fig. 3a, both evolutions are illustrated for one point on the outer lateral surface of the cylinder. In the first 10 seconds, the temperature decreases rapidly, until the process reaches a final state around $t = 60$ s. When the temperature falls below $\theta_{\mathrm{Ms}} = 196.96$ °C, martensite starts to evolve. In the end, a stationary martensitic volume fraction $c^{\mathrm{M}} = 0.87$ is

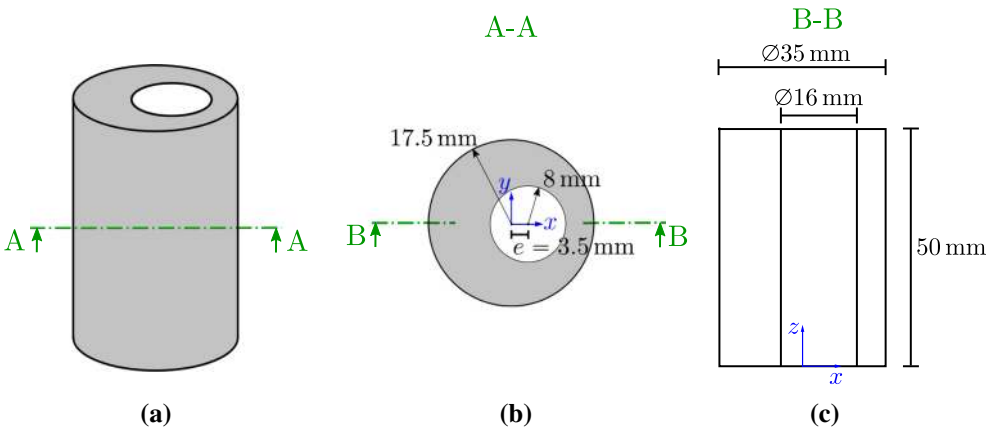

Fig. 1 **a** Cylindrical specimen with eccentric hole and its dimensions **b** in horizontal cut A-A and **c** in vertical cut B-B

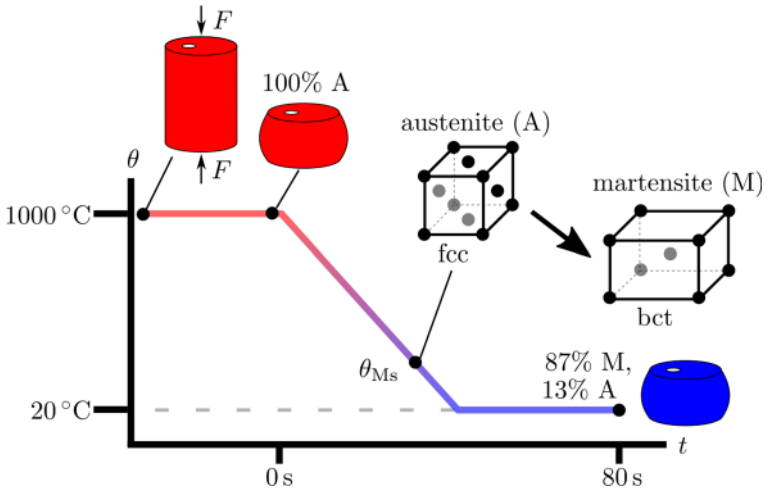

Fig. 2 Schematic representation of the hot forming process and the subsequent cooling period of the cylindrical specimen with the occurring phase transformation of the considered chromium-alloyed steel 1.3505 (100Cr6). The simulated period of the complete hot forming process lasts from 0 to 80 s

reached. For the use in computations, the martensitic volume fraction is fitted to a quadratic function dependent on the actual temperature θ based on the simulative data given by IFUM. Thus, the decrease in the austenitic volume fraction c^{A} after reaching the martensitic start temperature θ_{Ms} can be described by Eq. (1), which is additionally depicted in Fig. 3b. The martensitic volume fraction is obtained from $c^{\mathrm{M}} = 1 - c^{\mathrm{A}}$.

$$c^{\mathrm{A}} = \begin{cases} 1 & \text{for } \theta > \theta_{\mathrm{Ms}}, \\ 1 - (85.7602 + 0.0471337\,\theta - 0.00244999\,\theta^2)/100 & \text{for } \theta \leq \theta_{\mathrm{Ms}}. \end{cases} \tag{1}$$

It has to be noticed that Eq. (1) as function of the temperature cannot be used for the description of altered cooling routes. Thereto, an incorporation of kinetic effects of phase transformation has to be considered. Furthermore, the interested reader is kindly referred to Behrens et al. [4] for details on the experimental and numerical background.

3 Multiscale finite element simulation

The occurring microscopic phase transformation in conjunction with the characterization of residual stresses on different scales motivates an analysis using a multiscale simulation environment. In this section, an approach for the numerical simulation of the process described in Sect. 2 is given.

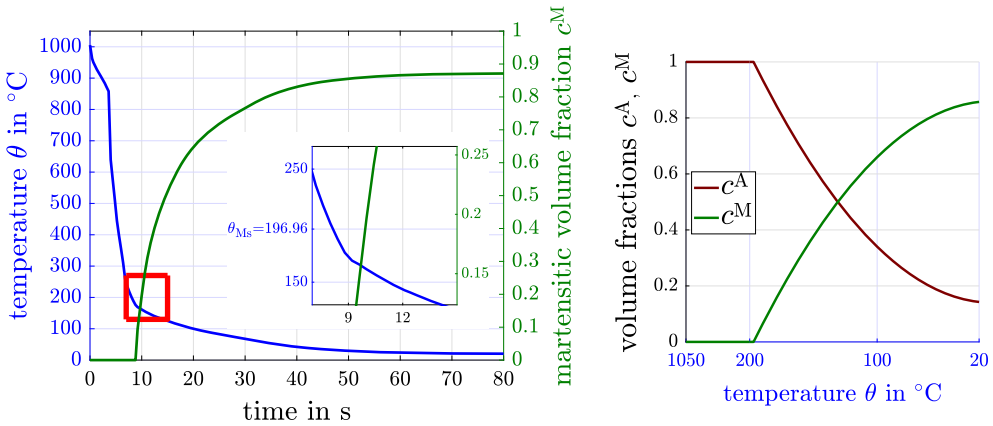

Fig. 3 **a** Temperature decrease on the outer lateral surface of the cylinder and related increase in martensitic volume fraction c^{M} in consequence of the cooling over a time range of 80 s with zoom in on the region, in which the phase transformation starts. **b** Temperature-dependent evolution of austenitic and martensitic volume fractions, c^{A} and c^{M}, respectively

Generally, different cooling procedures from a full austenitic state can result in multiple phases in the cooled part, e.g., pearlite, martensite, austenite, ferrite or bainite. In the following, austenite and martensite are considered since these are the occurring material phases in the examined cooling process, described in Sect. 2. Both phases on the microscale are modeled using an elasto-plastic material model at small strains based on the free energy function ψ following Miehe [24], Simo and Miehe [41], Simo and Hughes [40]

$$\psi(\boldsymbol{\varepsilon}^{\mathrm{e}}, e; \theta) = \underbrace{\frac{1}{2}\kappa\,(\operatorname{tr}\boldsymbol{\varepsilon}^{\mathrm{e}})^2 + \mu\,\|\operatorname{dev}\boldsymbol{\varepsilon}^{\mathrm{e}}\|^2}_{\text{elastic}} + \underbrace{\frac{1}{2}\,h\,e^2}_{\text{plastic}} - \underbrace{c_\rho\left(\theta\ln\frac{\theta}{\theta_0} - \theta + \theta_0\right)}_{\text{thermal}} - \underbrace{3\,\alpha_{\mathrm{T}}\,\kappa\,(\theta-\theta_0)\operatorname{tr}\boldsymbol{\varepsilon}^{\mathrm{e}}}_{\text{coupling}} \tag{2}$$

and the von Mises yield criterion Φ

$$\Phi = \|\operatorname{dev}\boldsymbol{\sigma}\| - \sqrt{\frac{2}{3}}\,y \le 0 \quad \text{with} \quad y = y_0 + \beta. \tag{3}$$

Therein, $\boldsymbol{\varepsilon}^{\mathrm{e}}$ is the elastic strain tensor, θ and θ_0 are the actual and initial temperature, respectively, and e is a strain-like internal variable. The present material parameters are the bulk modulus κ, shear modulus μ, heat expansion coefficient α_{T} and linear hardening parameter h. For the product of specific heat capacity c and density ρ, the abbreviation c_ρ is introduced. Later on, h is approximated by piecewise linear interpolation of a nonlinear yield curve, depending on θ and e, see Sect. 3.3. There, a linear interpolation scheme for the material parameters within the actual time step is given based on the constant temperature θ_n from the previous time step, since it ensures numerical stability, see also Sect. 3.2. Therein, this strain-like variable e can be interpreted as accumulated plastic strains which are defined following Simo and Hughes [40]

$$e = \int_0^t \sqrt{\frac{2}{3}}\,\|\dot{\boldsymbol{\varepsilon}}^{p}(\hat{t})\|\,\mathrm{d}\hat{t} \tag{4}$$

with t as actual time and $\dot{\boldsymbol{\varepsilon}}^{p}$ as plastic strain rate. Moreover, the initial and actual yield stresses, y_0 and y, are related by the stress-like work conjugate to e defined as β. By the evaluation of the entropy inequality the stresses $\boldsymbol{\sigma}$ are related to the elastic strains $\boldsymbol{\varepsilon}^{\mathrm{e}}$ via the free energy function, i.e., $\boldsymbol{\sigma} = \partial_{\boldsymbol{\varepsilon}^{\mathrm{e}}}\psi$, and $\beta = \partial_e\psi$.

For the numerical modeling, a two-scale finite element simulation is used, see Miehe et al. [26], Schröder [39]. In the following, the occurring macroscopic quantities are indicated by $\bar{\bullet}$ and microscopic ones by $\bullet$. On

the macroscale, a 2D boundary value problem (BVP) is considered with a one-way coupled thermo-elasto-plastic material behavior, neglecting the effects of latent heat. The differential equations balance of momentum and balance of energy in the absence of outer forces and heat sources, i.e.,

$$\operatorname{div} \bar{\boldsymbol{\sigma}} = \mathbf{0} \quad \text{and} \quad \bar{\rho}\, \dot{\bar{\epsilon}} - \bar{\boldsymbol{\sigma}} : \dot{\bar{\boldsymbol{\varepsilon}}} + \operatorname{div} \bar{\boldsymbol{q}} = 0\,, \tag{5}$$

have to be solved. The occurring macroscopic quantities are the density $\bar{\rho}$, the rate of the specific internal energy $\bar{\epsilon}$, the stresses $\bar{\boldsymbol{\sigma}}$, the strain rate $\dot{\bar{\boldsymbol{\varepsilon}}}$ and the heat flux vector $\bar{\boldsymbol{q}}$, which is computed by $\bar{\boldsymbol{q}} = -\bar{k}\, \operatorname{grad} \bar{\theta}$ with the heat conduction coefficient $\bar{k}$.

Furthermore, the macroscopic boundary conditions are described by

$$\begin{aligned} \bar{\boldsymbol{u}} &= \bar{\boldsymbol{u}}_0 \text{ on } \partial\mathcal{B}_{\bar{\boldsymbol{u}}}\,, & \bar{\boldsymbol{t}} &= \bar{\boldsymbol{\sigma}} \cdot \bar{\boldsymbol{n}} \text{ on } \partial\mathcal{B}_{\bar{\boldsymbol{t}}}\,, \\ \bar{\theta} &= \bar{\theta}_0 \text{ on } \partial\mathcal{B}_{\bar{\theta}}\,, & \bar{q}_0 &= \bar{\boldsymbol{q}} \cdot \bar{\boldsymbol{n}} \text{ on } \partial\mathcal{B}_{\bar{\boldsymbol{q}}}\,. \end{aligned} \tag{6}$$

with displacement vector $\bar{\boldsymbol{u}}$, traction vector $\bar{\boldsymbol{t}}$ normal vector $\bar{\boldsymbol{n}}$ and heat flux $\bar{q}_0$ on the boundary. For the boundaries, it must hold that

$$\begin{aligned} \partial\mathcal{B}_{\bar{\boldsymbol{u}}} \cup \partial\mathcal{B}_{\bar{\boldsymbol{t}}} &= \partial\mathcal{B}\,, & \partial\mathcal{B}_{\bar{\boldsymbol{u}}} \cap \partial\mathcal{B}_{\bar{\boldsymbol{t}}} &= \emptyset\,, \\ \partial\mathcal{B}_{\bar{\theta}} \cup \partial\mathcal{B}_{\bar{\boldsymbol{q}}} &= \partial\mathcal{B}, & \partial\mathcal{B}_{\bar{\theta}} \cap \partial\mathcal{B}_{\bar{\boldsymbol{q}}} &= \emptyset\,. \end{aligned} \tag{7}$$

On the microscale, a 2D isothermal elasto-plastic BVP is considered under the assumption that a vanishing temperature gradient inside each microscopic BVP can be used. A representative volume element (RVE) is used to represent the microstructure of the material. On the microscale, the balance of momentum $\operatorname{div} \boldsymbol{\sigma} = \mathbf{0}$ is solved using periodic boundary conditions.

Based on the solution of the microscopic BVP, the macroscopic moduli $\bar{\mathbb{C}}$ and macroscopic stresses $\bar{\boldsymbol{\sigma}}$ are computed by a numerical homogenization scheme based on the microscopic moduli $\mathbb{C}$ and stresses $\boldsymbol{\sigma}$, cf. Miehe et al. [25]

$$\bar{\boldsymbol{\sigma}} = \frac{1}{V} \int_{\mathrm{RVE}} \boldsymbol{\sigma}\, \mathrm{d}v\,, \quad \bar{\mathbb{C}} := \partial_{\bar{\varepsilon}}\, \bar{\boldsymbol{\sigma}} = \frac{1}{V} \int_{\mathrm{RVE}} \partial_{\bar{\varepsilon}}\, \boldsymbol{\sigma}(\varepsilon)\, \mathrm{d}v\,. \tag{8}$$

Furthermore, the macroscopic quantities $\bar{\mathcal{P}}$ necessary for the solution of the energy balance equation are computed by volume averaging, i.e., the microscopic material parameters $\mathcal{P}$ have to be weighted with the current volume fractions of austenite c^{A} and martensite c^{M}

$$\bar{\mathcal{P}} = c^{\mathrm{A}}\, \mathcal{P}^{\mathrm{A}} + c^{\mathrm{M}}\, \mathcal{P}^{\mathrm{M}} \quad \text{for } \mathcal{P} \in \{\kappa, k, c_\rho, \alpha_{\mathrm{T}}\}. \tag{9}$$

For further information regarding the direct micro–macro-transition scheme, the interested reader is kindly referred to Miehe et al. [26], Schröder [39] among others.

3.1 Setup of the boundary value problem

For the numerical analysis, a cross section of the cylindrical specimen applying plane strain conditions is considered. Its dimensions are given in Fig. 4. As simplification, only two parts of the axial section are modeled, which represent the thin and thick side and are defined with an opening angle $2\,\alpha = 10\,^\circ$. Due to the eccentricity of the hole, the inner lateral surface and the outer one are not coaxial.

Dirichlet boundary conditions are used to apply the cooling, as shown in Fig. 3, on $\partial\mathcal{B}_{\bar{\theta}}$ of the macroscale BVPs representing thin and thick side of the cylinder. By cooling over the lateral surface, it is assumed that the heat flux in circumferential direction only has minor impact, and thus, $\bar{q}_0 = 0$ on boundary $\mathcal{B}_{\bar{\boldsymbol{q}}}$ is applied. For simplification, rotational symmetry is considered, although it is not given, so that all nodal displacements on $\partial\mathcal{B}_{\bar{\boldsymbol{u}}}$ are fixed orthogonal to the radial cuts, see Fig. 5.

The symmetry of both boundary value problems is not further exploited to obtain more precise results regarding the stress analysis, which will be done along the x-axis for $y = 0$. Using the given configuration, integration points, for which the stresses are assessed, are positioned along this axis. Exploitation of the symmetry would change that insofar, that not integration points but nodes would lie on the x-axis with $y = 0$. Thus, an additional extrapolation would be required to compute the stresses at the nodes, which would result in an additional interpolation.

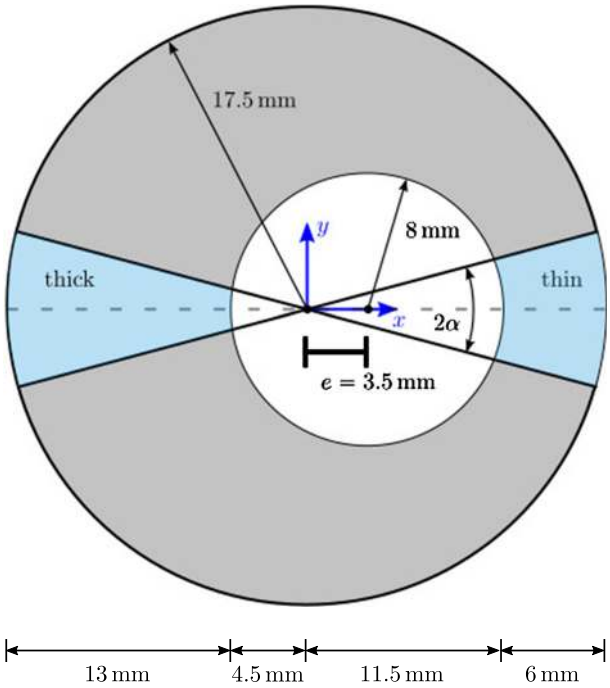

Fig. 4 Geometry to analyze the cooling of the lateral surface of a cylinder inducing phase transformation and therewith resulting in residual stresses

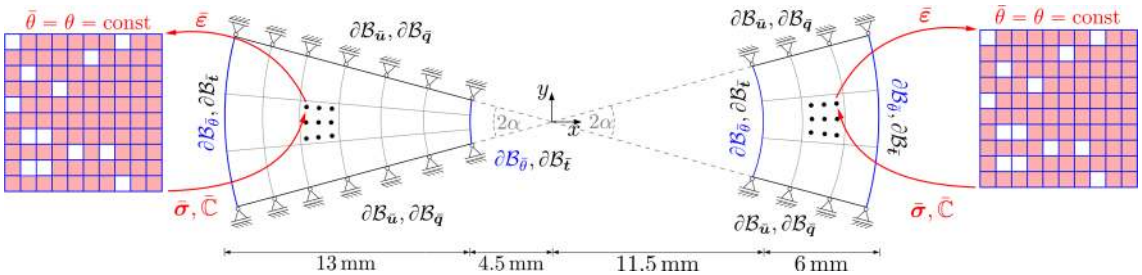

Fig. 5 Two macroscopic boundary value problems are analyzed, depicting thick and thin cylindrical section with shown Dirichlet boundary $\partial\mathcal{B}_{\bar{\boldsymbol{u}}}$, $\partial\mathcal{B}_{\bar{\theta}}$ and Neumann boundary $\partial\mathcal{B}_{\bar{\boldsymbol{t}}}$, $\partial\mathcal{B}_{\bar{\boldsymbol{q}}}$. Cooling over the lateral surface $\partial\mathcal{B}_{\bar{\theta}}$ (blue), the microscopic mesh with final phase distribution, martensite in red and austenite in white, are shown

3.2 Modeling of the austenite-to-martensite phase transformation

The phase transformation from austenite to martensite is considered through a temperature-dependent evolution of the volume fractions c^{A} and c^{M}. In order to avoid fluctuations in this measure, the macroscopic temperature $\bar{\theta}_n$ from the previous time step t_n is directly transferred to the microscopic level as state variable $\theta_n = \bar{\theta}_n \,\forall \boldsymbol{x} \in \mathrm{RVE}$ in the current time step $n+1$. Based thereon, the volume fractions of austenite $c^{\mathrm{A}}(\theta_n)$ and martensite $c^{\mathrm{M}}(\theta_n)$ as well as the material parameters are determined. Initially, there is 100% austenite, i.e., $c^{\mathrm{A}} = 1$. After cooling below the martensitic start temperature θ_{Ms}, martensite starts to form and the phase fraction of austenite decreases. To represent this process, an element-wise switch of the related material is carried out. Based on the martensitic volume fraction $c^{\mathrm{M}} = 1 - c^{\mathrm{A}}$, a section of the finite elements is randomly identified to be martensite. In the final state, there is 87% martensite and 13% austenite, which results in the exemplary distribution shown in red and white, respectively, in Fig. 5. It has to be noticed that there is no difference in the final volume fractions, whether a material point at the bulk material or near the surface is considered. The applied cooling route results in an almost uniform phase distribution as obtained in simulation at the IFUM. When switching from austenite to martensite, a volume expansion of 2% of the martensitic phase is applied to represent the change from fcc to bct lattice, as described in Sect. 2. It is incorporated as $\varepsilon^{*}_{\mathrm{vol}} = 0.02$ as shown in Table 1. Afterwards, a classical radial return algorithm for the von Mises yield criterion is applied to

Table 1 Solution of microscopic BVP

(I)	Get macroscopic temperature $\theta_n = \bar{\theta}_n \; \forall \boldsymbol{x} \in \text{RVE}$, initialize $\varepsilon^*_{\text{vol}} = 0$ Get material parameters for austenite/martensite by interpolation based on θ_n, see Sect. 3.3: $\kappa, \mu, k, c_\rho, \alpha_\text{T}, y, h$
(II)	Compute austenitic volume fraction $c^\text{A}(\theta_n)$ using Eq. (1)
(III)	Add random elements to martensitic domain $\mathcal{B}^\text{M}$ such that $c^\text{M} \approx \frac{1}{V} \int_{\mathcal{B}^\text{M}} \text{d}V$ with total volume V of RVE Set $\varepsilon^*_{\text{vol}} = 0.02$ for $\mathcal{B}^\text{M}$
(IV)	Compute total strains $\forall \boldsymbol{x} \in \text{RVE}$ $\boldsymbol{\varepsilon} = \nabla_s \boldsymbol{u} - \varepsilon^*_{\text{vol}} \mathbf{1}$ with $\nabla_s \boldsymbol{u} := \frac{1}{2}(\nabla \boldsymbol{u} + \nabla^\text{T} \boldsymbol{u})$
(V)	Solve div $\boldsymbol{\sigma} = \mathbf{0}$ while satisfying $\Phi = \Vert \text{dev}\, \boldsymbol{\sigma} \Vert - \sqrt{\frac{2}{3}} y \leq 0$
(VI)	Compute macroscopic moduli $\bar{\mathbb{C}}$ and stresses $\bar{\boldsymbol{\sigma}}$, see Eq. (8)

calculate the microscopic material response, see Simo and Hughes [40]. The solution steps of the microscopic BVP are summarized in Table 1.

3.3 Interpolation of microscopic material parameters

The numerical modeling of the cooling process includes the setup of an appropriate material model and the calibration of material parameters. Therefore, the Institute of Forming Technology and Machines, Leibniz University Hannover, (IFUM) provides data, which is obtained using the thermodynamic simulation software JMatPro [10]. Therewith, mechanical and thermal material parameters are calculated based on the chemical composition of the considered Cr-alloyed steel 1.3505 (100Cr6), which is given in Table 2. As stated in Sect. 3.2, the macroscopic temperature θ_n is passed onto the microscale as state variable, what matches the assumption of an isothermal mechanical problem on the minor scale. The provided data are evaluated with respect to that state variable as describes in the following.

The data are generated in a temperature range from 50 to 950 °C with step size 50 °C for each material phase. The Young's modulus E, the Poisson's ratio ν, the heat conduction coefficient k, the product of specific heat capacity and density c_ρ and the heat expansion coefficient α_T are provided as function of the temperature θ. Furthermore, the yield stress y is given depending on the accumulated plastic strains e for specific temperatures.

A first dataset provides information of the mechanical material parameters, namely E and ν, used to derive bulk modulus κ and shear modulus μ, and thermal material parameters k, c_ρ and α_T. These parameters determine the material behavior for the elastic regime. The data are piecewise linear interpolated for the thermal and mechanical material parameters between the sampling points. The results are plotted in Fig. 6.

For the plastic regime, a second dataset provides the yield stress y dependent on the accumulated plastic strains $e \in [0, 4]$ for certain temperatures $\theta \in [50\,°\text{C}, 1050\,°\text{C}]$. It is obtained in dilatometer tests using a strain rate of $\dot{\boldsymbol{\varepsilon}} = 0.001\,\text{s}^{-1}$. The data for θ are given in equidistant steps of 50 °C but for e non-equidistant, i.e., the step sizes are

$$\begin{aligned} 0.02 &\text{ for } e \in [0, 0.3], & 0.5 &\text{ for } e \in [1, 2], \\ 0.1 &\text{ for } e \in [0.3, 1], & 1 &\text{ for } e \in [2, 4]. \end{aligned} \tag{10}$$

Note that, JMatPro provides in general data for the accumulated plastic strains in a range of [0, 4] but for the considered cooling process of a thick-walled steel part, only small strains are expected. In order to obtain the model parameters y and h with respect to the current temperature θ_n, a piecewise two step linear interpolation

Table 2 Chemical composition in volume percent of the investigated steel alloy 1.3505 (100Cr6) used for material data generation with JMatPro

	C	Si	Mn	P	S	Cr	Mo	Fe
100Cr6	0.99	0.25	0.35	0.025	0.015	1.475	0.1	Balance

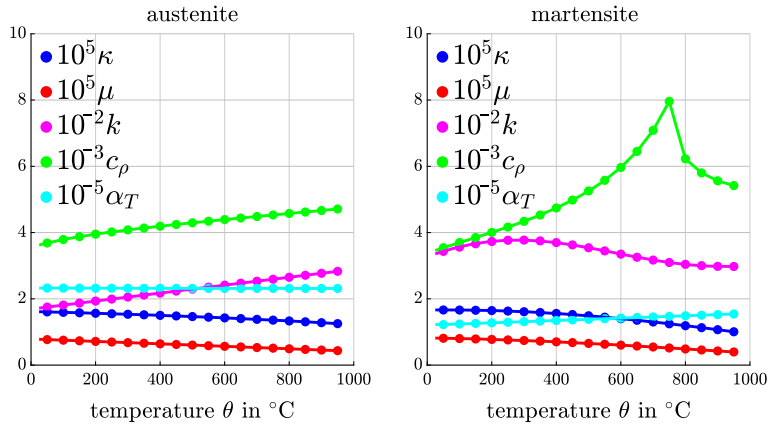

Fig. 6 Sampling points and piecewise linear interpolation **a** for austenite and **b** martensite: bulk modulus κ in MPa, shear modulus μ in MPa, heat conduction coefficient k in J/(mm s K), product of specific heat capacity and density c_ρ in N/(K mm)^2 and heat expansion coefficient α_T in 1/K

Table 3 Provided data for the interpolation of yield stress y and linear hardening parameter h based on temperature θ and accumulated plastic strains e

	...	θ_{i-1}	θ_i	...
$\vdots$		$\vdots$	$\vdots$	
e_{j-1}	...	$y_{j-1,i-1}$	$y_{j-1,i}$	...
e_j	...	$y_{j,i-1}$	$y_{j,i}$	...
$\vdots$		$\vdots$	$\vdots$	

is used within the numerical simulation. Therefore, the material parameters depend on current temperature θ_n and accumulated plastic strains e_n at one microscopic material point. Both quantities are used to determine the rows and columns in Table 3 of the provided data that has to be interpolated, i.e., $\theta_{i-1} \leq \theta_n < \theta_i$ and $e_{j-1} \leq e_n < e_j$.

The first interpolation step is done row-wise along the temperature. Based on $(\theta_{i-1}, y_{j-1,i-1})$ and $(\theta_i, y_{j-1,i})$ an interpolated value $y(e_{j-1}, \theta_n)$ is computed using Eq. $(11)_1$. Analogously, $y(e_j, \theta_n)$ is computed between $(\theta_{i-1}, y_{j,i-1})$ and $(\theta_i, y_{j,i})$, cf. Eq. $(11)_2$. Afterwards, the results $y(e_{j-1}, \theta_n)$ and $y(e_j, \theta_n)$ are used to interpolate the sought value $y(e_n, \theta_n)$ in a second step, cf. Eq. $(11)_3$. Here, the linear hardening parameter h is obtained as the slope of the linear relation in Eq. $(11)_3$.

$$
\begin{aligned}
y(e_{j-1}, \theta_n) &= y_{j-1,i-1} + \frac{y_{j-1,i} - y_{j-1,i-1}}{\theta_i - \theta_{i-1}} (\theta_n - \theta_{i-1}) \,, \\
y(e_j, \theta_n) &= y_{j,i-1} + \frac{y_{j,i} - y_{j,i-1}}{\theta_i - \theta_{i-1}} (\theta_n - \theta_{i-1}) \,, \\
y(e_n, \theta_n) &= y(e_{j-1}, \theta_n) + \underbrace{\frac{y(e_j, \theta_n) - y(e_{j-1}, \theta_n)}{e_j - e_{j-1}}}_{=h} (e_n - e_{j-1}) \,.
\end{aligned}
\tag{11}
$$

This interpolation scheme is applied for the yield stress of austenite and martensite. Since martensite starts to form below a temperature of 200 °C, a temperature range from 20 to 200 °C is considered here. In contrast, austenite is present at all temperatures of the cooling process, such that the full temperature range is evaluated. Values for y and h for different temperatures and accumulated plastic strains are exemplary given in Fig. 7.

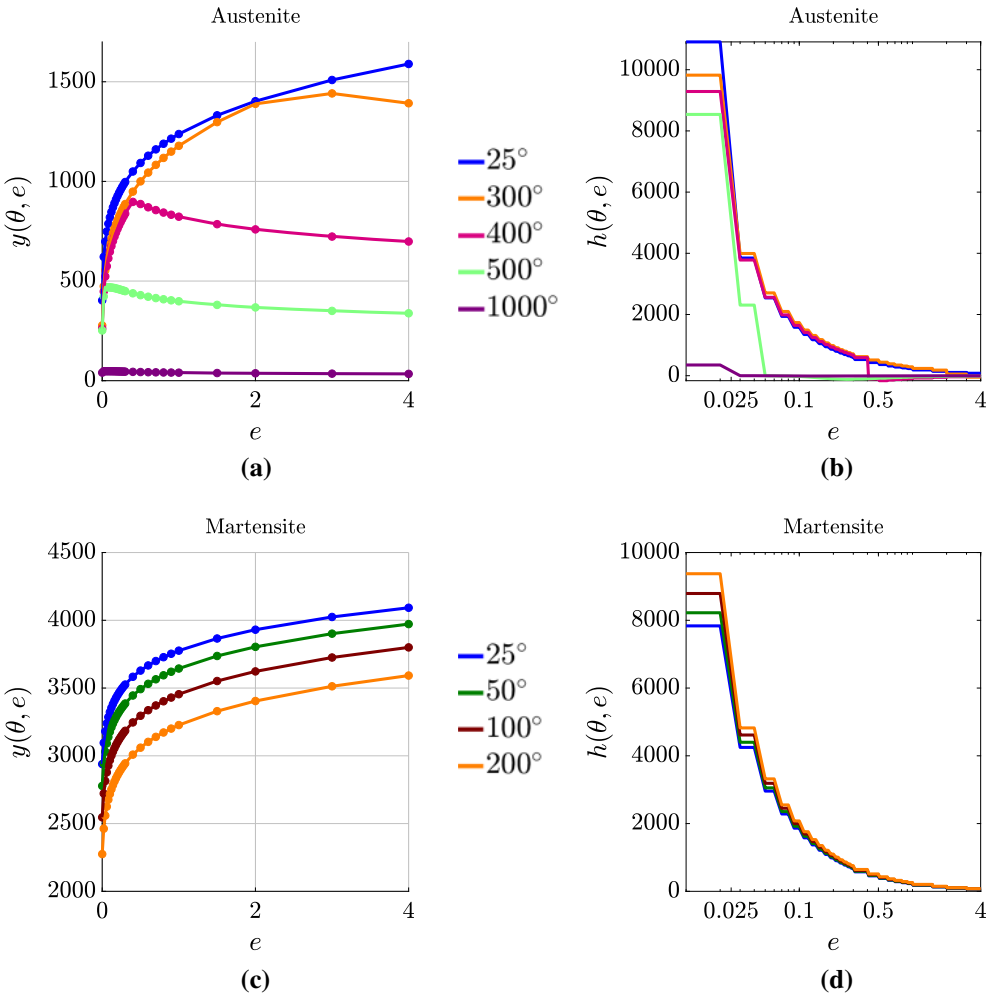

Fig. 7 Results of interpolation of material data for austenite and martensite: **a**, **c** yield stress $y(\theta, e)$ in MPa compared to the given data points and **b**, **d** linear hardening parameter $h(\theta, e)$ in MPa in logarithmic scale

4 Numerical examples

In the previous sections, a model to incorporate the austenite-to-martensite phase transformation in a two-scale finite element simulation has been introduced. All necessary data have been provided based on experimental and simulative information to compute the cooling detached from the forming of a two-dimensional cylindrical section, which has been defined in Sect. 3.1. On the macroscale, 9-noded quadrilateral finite elements are chosen for discretization, while the microscopic BVP is discretized using 4-noded quadrilateral finite elements in a structured mesh. Besides the cooling on the boundary $\partial\mathcal{B}_{\bar{\theta}}$, no outer forces are applied. Hence, this two-scale finite element simulation enables the computation of stresses that can be interpreted as residual stresses.

In the following, the influence of the macroscopic and microscopic mesh density on the stress distribution is examined. Moreover, the time step size as well as the cooling rate are varied. The focus of the analysis is directed toward the tangential stress distribution, since these stresses are most relevant with respect to strength and durability of the final component. The evaluation of the stresses σ_{yy} along the x-axis for $y = 0$ provides the tangential residual stresses. In Table 4, an overview of the different meshes in the analysis of mesh density is given and the abbreviation is explained. Therein, the mesh is refined only in radial direction according to the cooling direction applied on the lateral surface. A refinement in circumferential direction with respect to the height does not show a great or even no influence.

Table 4 Overview of the analyzed combination of macroscopic and microscopic discretization (width and height) and explanation of the used abbreviation

Macroscopic mesh Elements Width	Height	Abbreviation	Microscopic mesh Elements Width	Height	Abbreviation	Notation
$\overline{10}$	$\overline{5}$	coarse $\overline{\text{C}}$	10	10	coarse C	$\overline{\text{C}}$C
			20	20	medium M	$\overline{\text{C}}$M
			30	30	fine F	$\overline{\text{C}}$F
$\overline{20}$	$\overline{5}$	medium $\overline{\text{M}}$	10	10	coarse C	$\overline{\text{M}}$C
			20	20	medium M	$\overline{\text{M}}$M
			30	30	fine F	$\overline{\text{M}}$F
$\overline{30}$	$\overline{5}$	fine $\overline{\text{F}}$	10	10	coarse C	$\overline{\text{F}}$C
			20	20	medium M	$\overline{\text{F}}$M
			30	30	fine F	$\overline{\text{F}}$F
$\overline{40}$	$\overline{5}$	$\overline{\text{FF}}$	30	30	fine F	$\overline{\text{FF}}$F
$\overline{50}$	$\overline{5}$	$\overline{\overline{\text{F}}}$	30	30	Fine F	$\overline{\overline{\text{F}}}$F

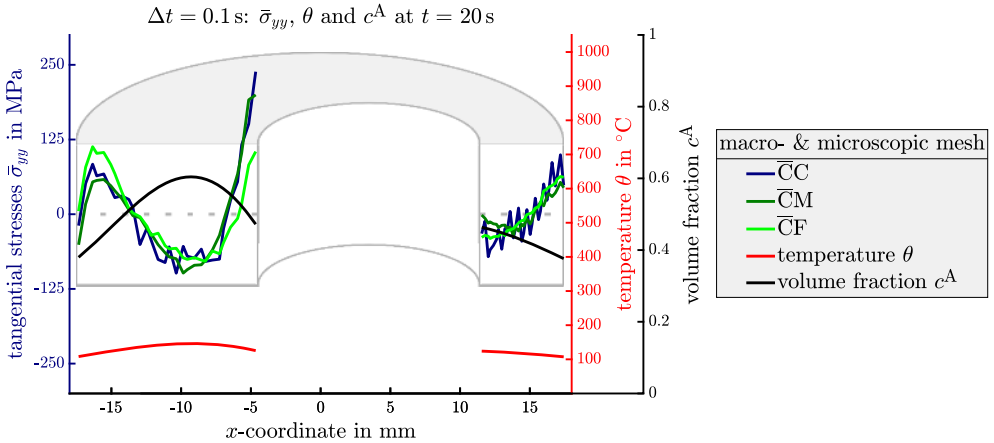

Fig. 8 Tangential stresses $\bar{\sigma}_{yy}$ for the x-axis at $y = 0$ and $t = 20\,\text{s}$ for macroscopically coarse discretization $\overline{\text{C}}$ and different microscopic meshes using time step size $\Delta t = 0.1\,\text{s}$

4.1 Study on macroscopic and microscopic mesh size

First, a constant time step size of $\Delta t = 0.1\,\text{s}$ is chosen for the complete cooling time of 80 s, in order to determine a reasonable macroscopic discretization. In Fig. 8, the stresses $\bar{\sigma}_{yy}$ for the x-axis at $y = 0$ and computational time $t = 20\,\text{s}$ are depicted for the coarsest macroscopic mesh size $\overline{\text{C}}$ and all three microscopic discretizations. Due to microstructural phenomena related to the ongoing phase transformation an unreasonable stress distribution can be observed independent of the microscopic mesh size. Hence, a refinement on the macroscale to a medium $\overline{\text{M}}$ or fine $\overline{\text{F}}$ mesh size needs to be analyzed. Figure 9 illustrates the stress distribution for those macroscopic meshes at time $t = 20\,\text{s}$. Obviously, a coarse microscopic discretization C does not show a reasonable stress distribution as it is indicated by the yellow $\overline{\text{M}}$C and green $\overline{\text{F}}$C curve.

Stresses computed by the other four combination of medium and fine macroscopic and microscopic discretization seem to be more suitable. Computations with a microscopically medium discretization $\overline{\text{M}}$M or $\overline{\text{F}}$M do not provide sufficiently smooth stress results, especially regarding the thin side BVP. Thus, the microscopic mesh should be further refined to mesh F. In order to decide between the two combination, i.e., $\overline{\text{M}}$F and $\overline{\text{F}}$F, it is inevitable to balance numerical costs with numerical accuracy. While the combination of both fine meshes $\overline{\text{F}}$F show best results, a greater number of BVPs have to be solved in every time step. At the same time, the stress plots for $\overline{\text{M}}$F do not show a strong deviation from $\overline{\text{F}}$F. Thus, in the following sections, these discretizations are considered on macroscale and microscale, respectively. As given in Fig. 10, a further refinement on the macroscale to discretizations $\overline{\text{FF}}$ or $\overline{\overline{\text{F}}}$ confirm the results of mesh size $\overline{\text{F}}$.

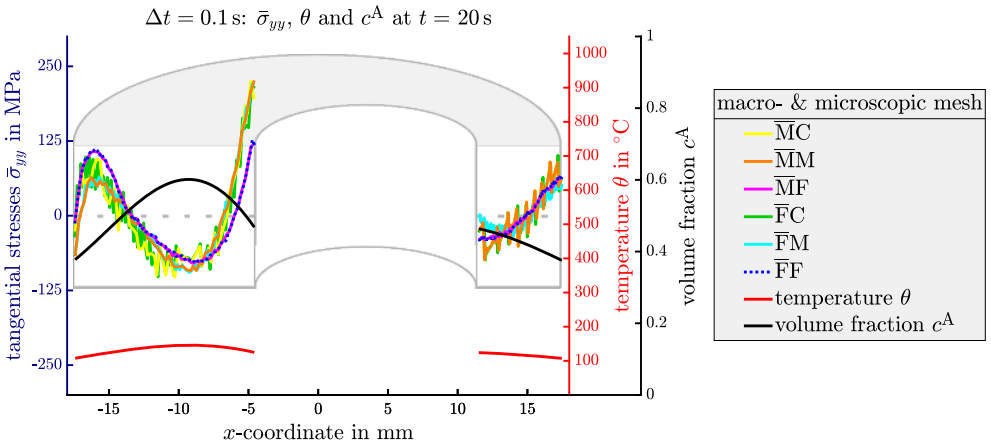

Fig. 9 Tangential stresses $\bar{\sigma}_{yy}$ for the x-axis at $y = 0$ and $t = 20\,\mathrm{s}$ for the discretization $\overline{\mathrm{M}}$ and $\overline{\mathrm{F}}$ of the macroscopic BVP and different microscopic meshes using time step size $\Delta t = 0.1\,\mathrm{s}$

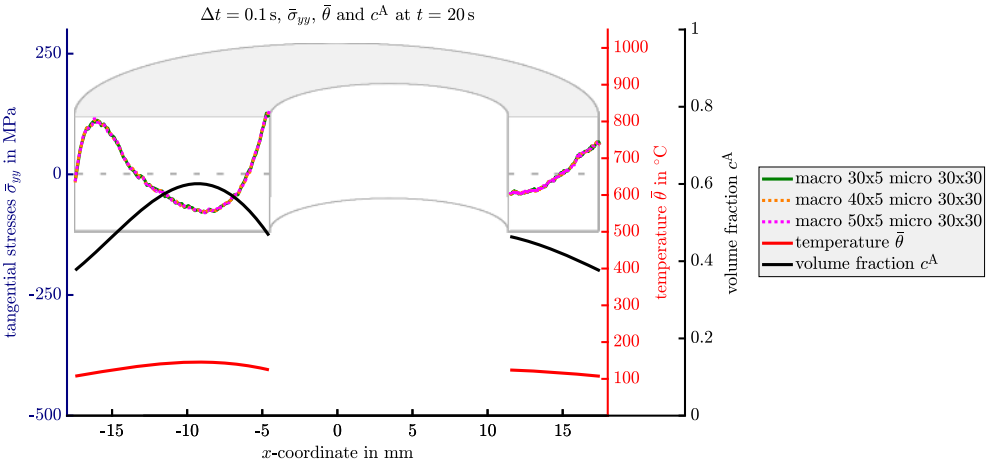

Fig. 10 Tangential stresses $\bar{\sigma}_{yy}$ for the x-axis at $y = 0$ and $t = 20\,\mathrm{s}$ for refined macroscopic meshes $\overline{\mathrm{F}}$, $\overline{\mathrm{FF}}$ or $\overline{\mathbb{F}}$ using time step size $\Delta t = 0.1\,\mathrm{s}$

4.2 Study on time step size

Mesh discretization $\overline{\mathrm{M}}\mathrm{F}$ is considered in the following analysis regarding the time step size. Therefore, the time step size is set to either $\Delta t = 0.5\,\mathrm{s}$ or $\Delta t = 1\,\mathrm{s}$ for the complete cooling time of 80 s. Additionally, the influence of the time stepping scheme especially during phase transformation is examined. Thus, a refinement of the time step size to $\Delta t = 0.05\,\mathrm{s}$ or $\Delta t = 0.01\,\mathrm{s}$ is applied between 8 and 40 s of computational time and remains $\Delta t = 0.1\,\mathrm{s}$ before and after this range.

One notices that larger time steps do not show convergence on the macroscale. A finer time stepping scheme does not significantly alter the results, cf. Fig. 11.

Note that for a discretization $\overline{\mathrm{M}}\mathrm{M}$ a refinement of the time step size can improve the results. In the previous Sect. 4.1 it has been discussed that a discretization does not show sufficiently smooth results, especially with respect to the thin side BVP. Choosing a time step size of $\Delta t = 0.05\,\mathrm{s}$ improves the smoothness of the stress distribution, whereas $\Delta t = 0.01\,\mathrm{s}$ does not lead do significant further improvement, see Fig. 12.

4.3 Evolution of tangential stresses

Using a suitable discretization as well as an appropriate time step size as determined in Sects. 4.1 and 4.2, the evolution of tangential stresses during the cooling process is investigated. Thus, in Figs. 13, 14 and 15, the tangential stresses $\bar{\sigma}_{yy}$ along the x-axis at $y = 0$ are given for meaningful points in time. It becomes

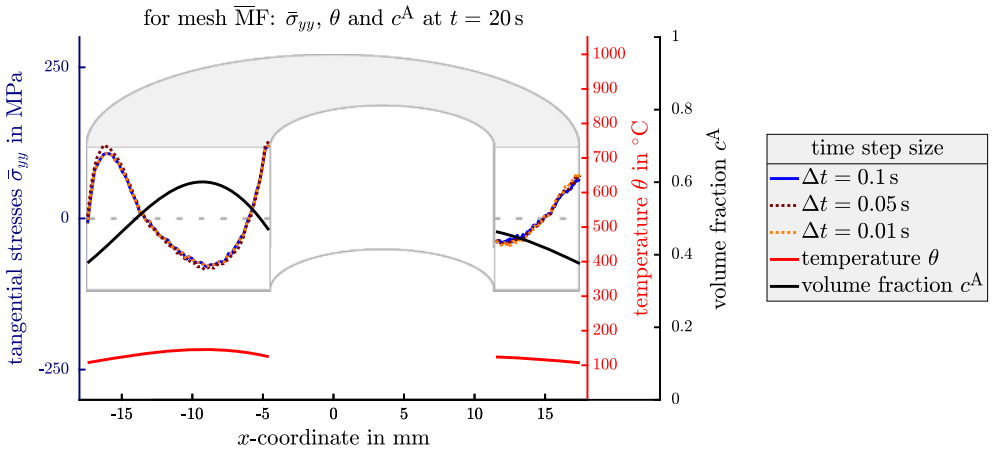

Fig. 11 Tangential stresses $\bar{\sigma}_{yy}$ for the x-axis at $y = 0$ and $t = 20\,\text{s}$ for the discretization $\overline{\text{MF}}$ and different time step sizes of $\Delta t \in \{0.1\,\text{s}, 0.05\,\text{s}, 0.01\,\text{s}\}$

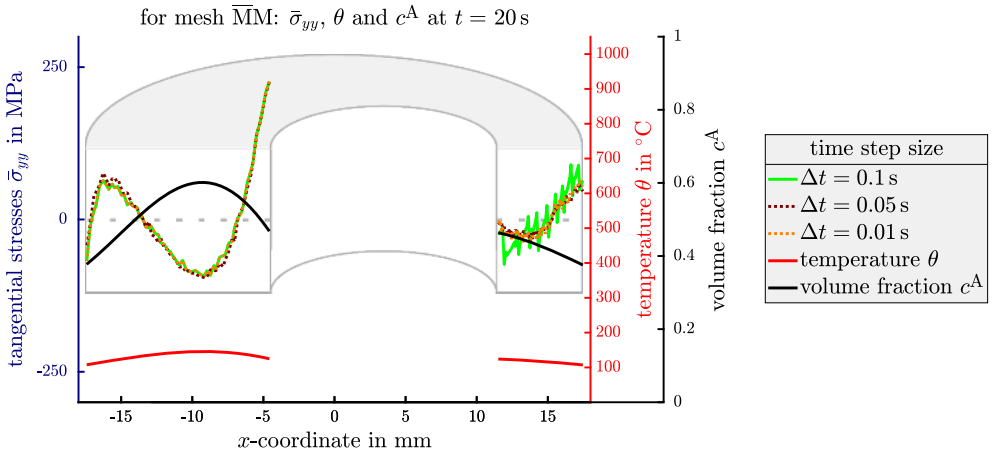

Fig. 12 Tangential stresses $\bar{\sigma}_{yy}$ for the x-axis at $y = 0$ and $t = 20\,\text{s}$ for the discretization $\overline{\text{MM}}$ and different time step sizes of $\Delta t \in \{0.1\,\text{s}, 0.05\,\text{s}, 0.01\,\text{s}\}$

possible to relate the stress development to the phenomena occurring in phase transformation such as the volume expansion of the unit cells. Based on this knowledge, the numerical environment enables a prediction of residual stress distributions for altered process parameters, e.g., cooling rate or cooling time.

Initially, the material 1.3505 (100Cr6) is a purely austenitic due to heating over 1000 °C. The cooling of the lateral surface of both—thick and thin—parts of the cylindrical specimen progresses slowly to the inner part of both geometries. It evokes small tensile stresses in the outer regions of the bodies. Naturally, the inner part of the thin side cool faster compared to the thick side. The stress distribution for $x \geq 15\,\text{mm}$ after 5 s of computation time show compressive stresses, see Fig. 13b.

After $t = 10\,\text{s}$, cf. Fig. 13c, the outer lateral surfaces are cooled below $\theta_{\text{Ms}} = 196.96\,°\text{C}$ and the phase transformation is initiated. It influences the tangential stresses clearly, as high compressive stresses occur due to the martensitic volume expansion. Once the temperature at inner and outer lateral surface of the thick side falls below the martensitic start temperature, compressive stresses evolve in those regions, see Fig. 13e, while the inner part shows tensile stresses. With ongoing phase transformation, the compressive stresses increase further, see Figs. 13f and 14c.

On the thin side, a different stress evolution can be observed. The outer lateral surface of the BVP is cooled faster than the inner lateral surface. The related temperature progress into the inner parts of the body evokes the phase transformation. Thus, compressive stresses are found at the outer lateral surface and in the inner parts, while tensile stresses occur at the inner lateral surface, see Fig. 13d. With initiation of the phase transformation on the inner lateral surface, a superposition of the previously introduced tensile stresses takes place and compressive stresses are observed, cf. Fig. 13e.

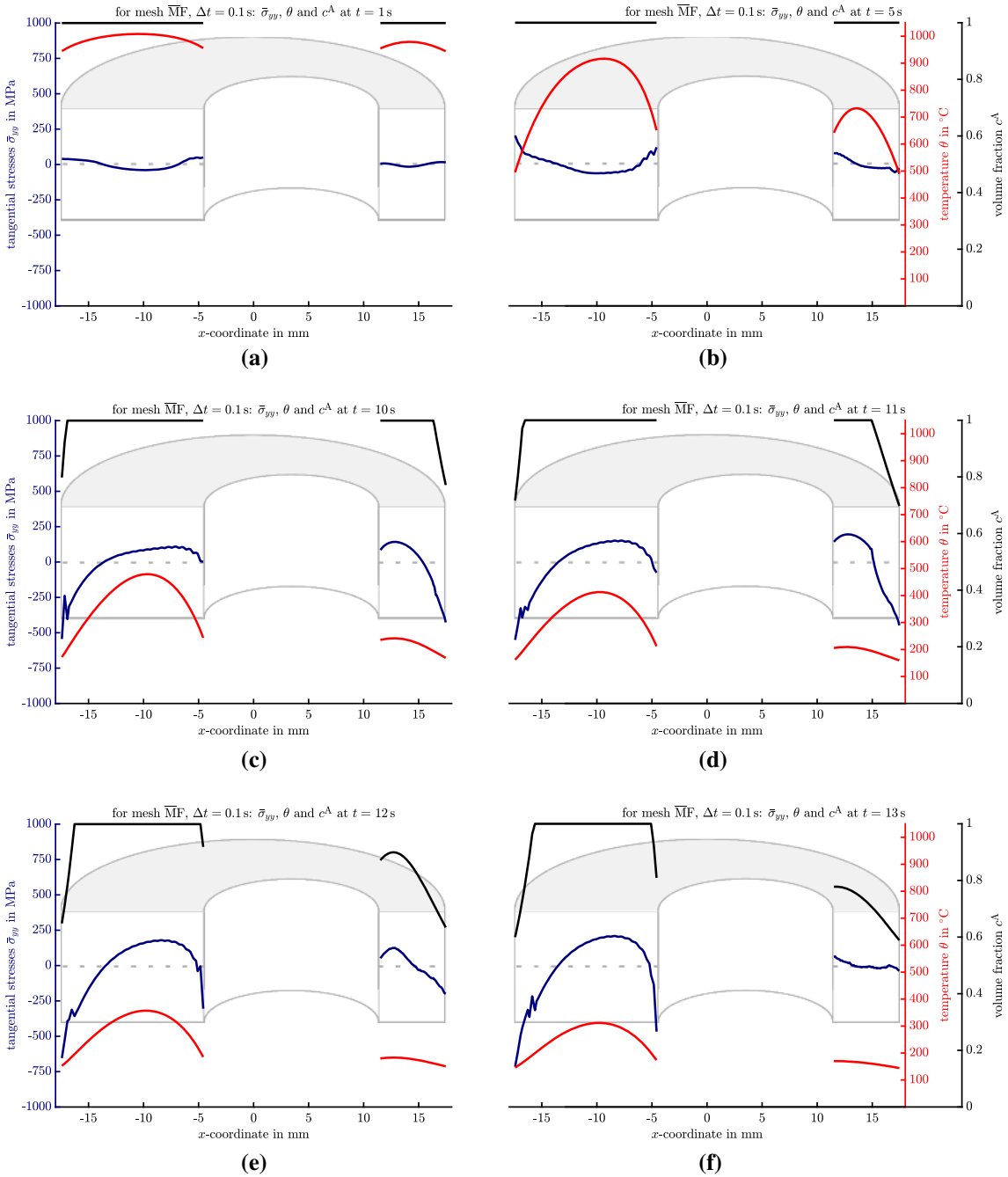

Fig. 13 Tangential stresses $\bar{\sigma}_{yy}$, temperature θ and austenitic volume fraction c^{A} for a macroscopic medium mesh $\overline{\mathrm{M}}$ and microscopic discretization F depicted at **a** $t = 1\,\mathrm{s}$, **b** $t = 5\,\mathrm{s}$, **c** $t = 10\,\mathrm{s}$, **d** $t = 11\,\mathrm{s}$, **e** $t = 12\,\mathrm{s}$ and **f** $t = 13\,\mathrm{s}$, step size $\Delta t = 0.1\,\mathrm{s}$

Qualitatively, this stress distribution remains, until a computation time of 17 s is reached, cf. Fig. 14d. At that time, the inner part of the thick side is subjected to phase transformation. Thereby, compressive stresses are evoked which affect the outer parts of the geometry, where at first the compressive stresses are reduced and later on turn over to tensile stresses, cf. Figs. 14e and 15c. For the thin side, the stresses distribution changes its sign as well, such that compressive stresses occur on the inner lateral surface, while tensile stresses can be found at the outer lateral surface, see Fig. 15d.

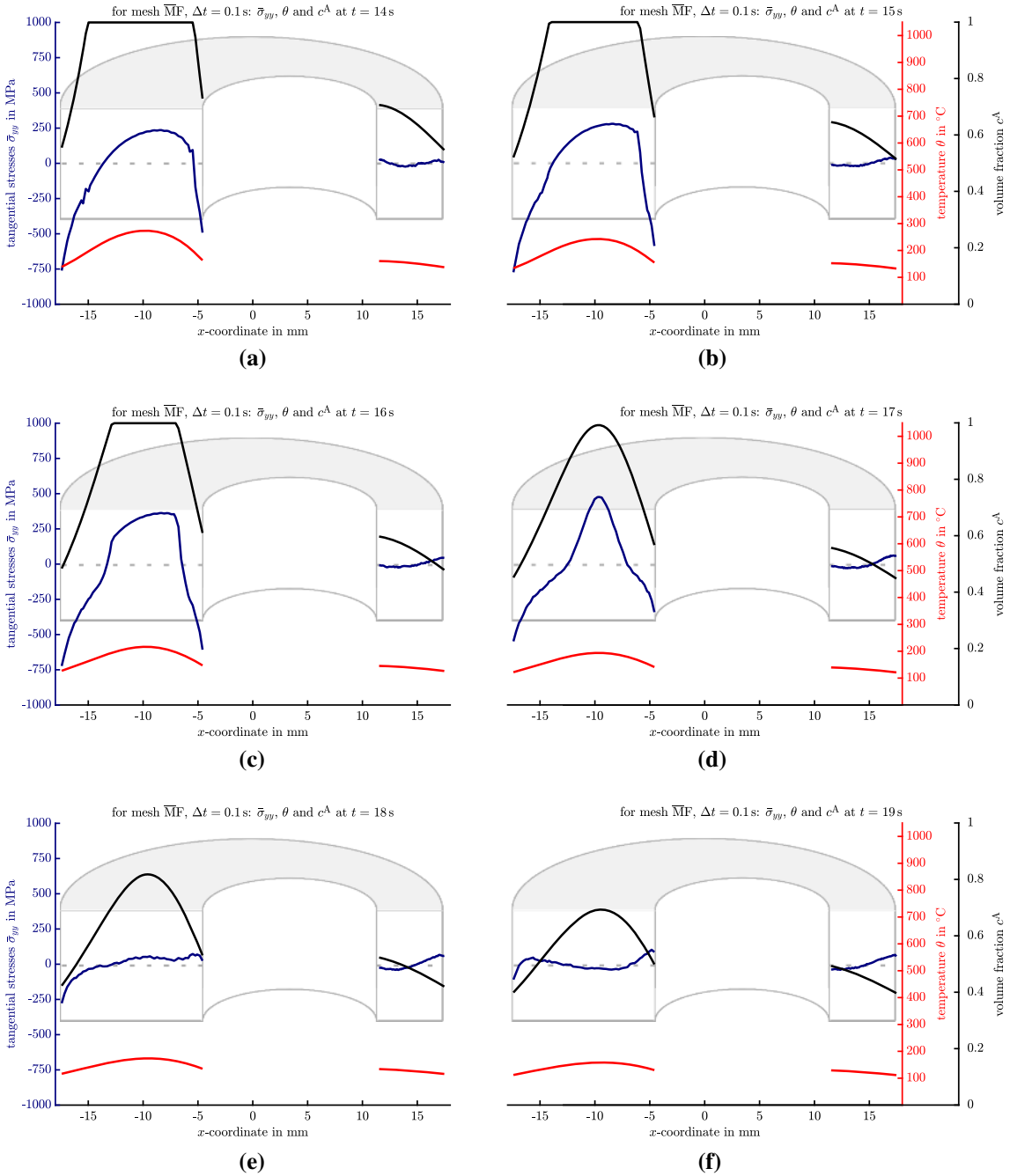

Fig. 14 Tangential stresses $\bar{\sigma}_{yy}$, temperature θ and austenitic volume fraction c^{A} for a macroscopic medium mesh $\overline{\mathrm{M}}$ and microscopic discretization F depicted at **a** $t = 14\,\mathrm{s}$, **b** $t = 15\,\mathrm{s}$, **c** $t = 16\,\mathrm{s}$, **d** $t = 17\,\mathrm{s}$, **e** $t = 18\,\mathrm{s}$ and **f** $t = 19\,\mathrm{s}$, step size $\Delta t = 0.1\,\mathrm{s}$

4.4 Principle study on the residual stress state for different cooling rates

For the use of targeted residual stress states to improve the components properties, compressive stresses in regions close to the surface seem reasonable. In the process simulation in Sect. 4.3, these only occur for the outer surface of the thin side boundary value problem. Thus, the cooling process has to be adapted, prospectively, such that the desired characteristics can be established. As a first attempt the total cooling time is altered in the following to analyze the influence of the final tangential stress distributions.

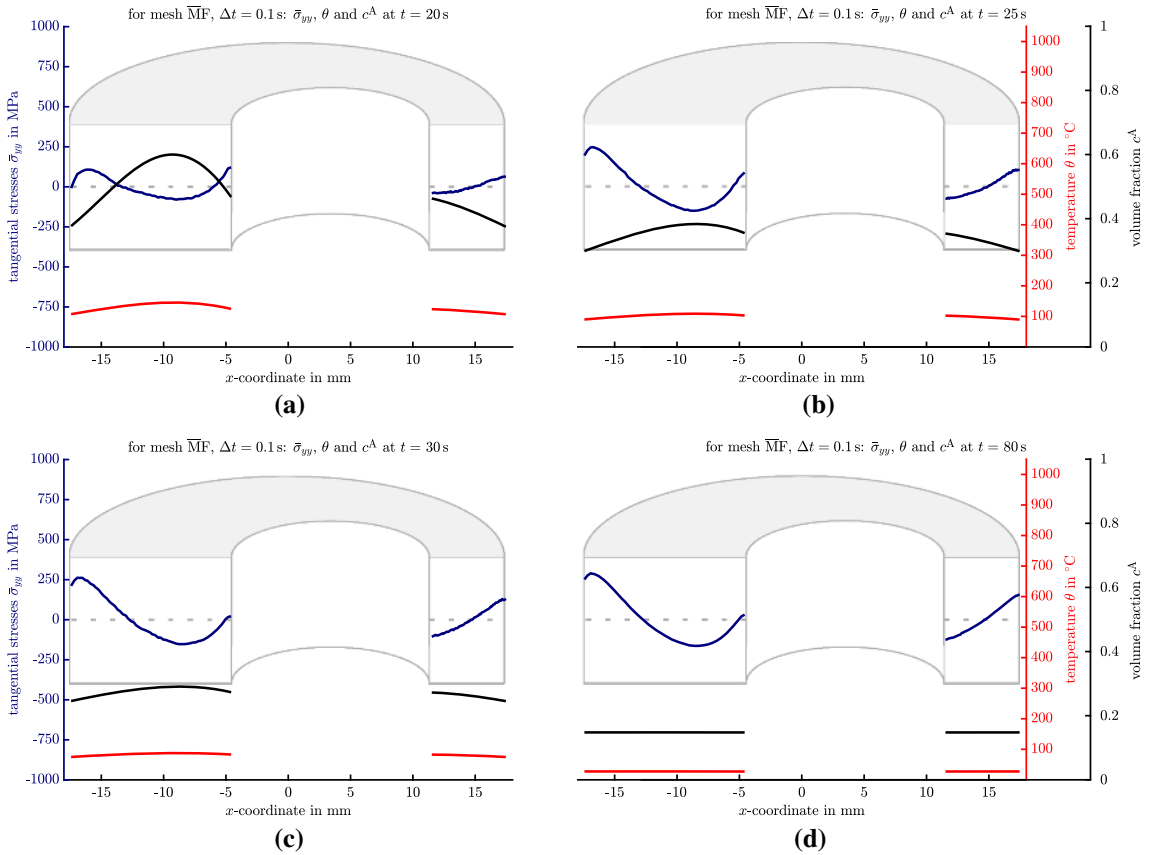

Fig. 15 Tangential stresses $\bar{\sigma}_{yy}$, temperature θ and austenitic volume fraction c^{A} for a macroscopic medium mesh $\overline{\mathrm{M}}$ and microscopic discretization F depicted at **a** $t = 20$ s, **b** $t = 25$ s, **c** $t = 30$ s and **d** $t = 80$ s, step size $\Delta t = 0.1$ s

Note that with assuming a simple scaling to shorten or lengthen the cooling time, no modification of the material parameters and microscopic constituents depending on the cooling rate is considered. Hence, neither additional phases such as pearlite, ferrite or bainite nor a varied function for the phase fraction, cf. Eq. (1), are taken into account in the following study. Thereby, the results presented in the following show the principle usability of the proposed numerical model; however, the above-mentioned modifications are inevitable to consider the changed parameter setup.

By changing the cooling time from 80 s to 40 s or 160 s by scaling the evolution of the temperature applied to the lateral surfaces, the cooling is fastened or slowed down, respectively, see Fig. 16a. The austenite-to-martensite phase transformation, which is directly related to temperature θ, is influenced and thereby, different stress distributions can be found. Shortening or extending the cooling time leads qualitatively to similar tangential stress curves. Quantitatively, a faster cooling during 40 s shows higher stresses than previous computation, while a slower cooling during 160 s results in lower stress values at the end of computation time, see Fig. 16b.

5 Conclusion

In this contribution, a numerical approach to analyze the cooling process of a cylindrical specimen has been presented. To incorporate microscopic phenomena, such as austenite-to-martensite phase transformation, which is associated with the cooling process, an application of a two-scale finite element simulation is proposed. It enables the computation of tangential stresses as consequence of the phase transformation. For the material model, a suitable calibration for the material parameters dependent on the temperature has been carried out. Studies regarding the mesh density as well the time stepping scheme have been presented, of which the results are summarized in Table 5. Here, only a qualitative but not quantitative analysis is performed, because the

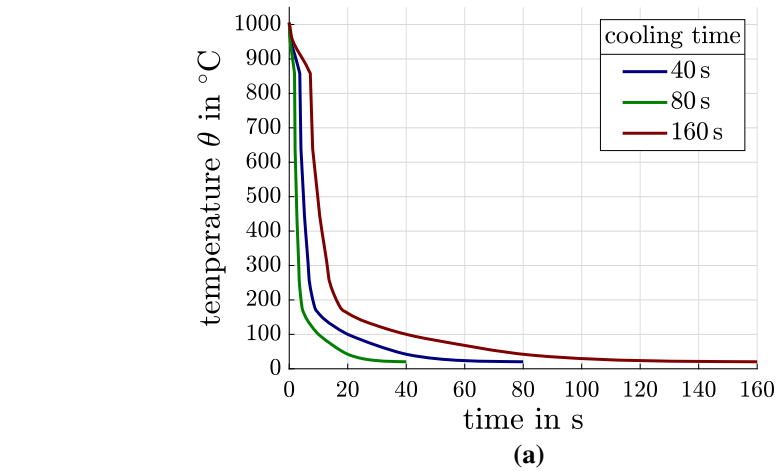

(a)

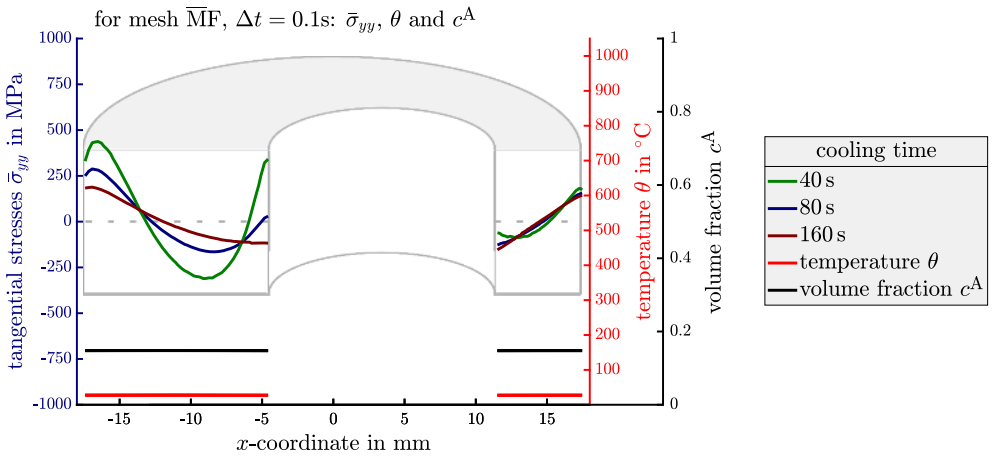

(b)

Fig. 16 **a** Scaling of the temperature evolution applied to to the lateral surface and **b** final distribution of tangential stresses $\bar{\sigma}_{yy}$, temperature θ and austenitic volume fraction c^{A} for a macroscopic medium mesh $\overline{\mathrm{M}}$ and microscopic discretization F are depicted for cooling time of 40 s, 80 s and 160 s, step size $\Delta t = 0.1$ s

Table 5 Differentiation into appropriate ⊕ or ineligible results ⊖ for macroscopic and microscopic discretizations, regarding notation, see Table 4, and time step sizes for an angle of $2\,\alpha = 10°$

Notation	Time step size Δt				
	1 s	0.5 s	0.1 s	0.1 s with refinement between 8 s and 40 s to 0.05 s	0.01 s
$\overline{\mathrm{C}}\mathrm{C}$	⊖	⊖	⊖	⊖	⊖
$\overline{\mathrm{C}}\mathrm{M}$	⊖	⊖	⊖	⊖	⊖
$\overline{\mathrm{C}}\mathrm{F}$	⊖	⊖	⊖	⊖	⊖
$\overline{\mathrm{M}}\mathrm{C}$	⊖	⊖	⊖	⊖	⊖
$\overline{\mathrm{M}}\mathrm{M}$	⊖	⊖	⊖	⊕	⊕
$\overline{\mathrm{M}}\mathrm{F}$	⊖	⊖	⊕	⊕	⊕
$\overline{\mathrm{F}}\mathrm{C}$	⊖	⊖	⊖	⊖	⊖
$\overline{\mathrm{F}}\mathrm{M}$	⊖	⊖	⊖	⊕	⊕
$\overline{\mathrm{F}}\mathrm{F}$	⊖	⊖	⊕	⊕	⊕

incorporation of effects such as latent heat requires an extension of the here presented numerical treatment. Furthermore, note that the residual stresses may change in long-term evolution due to stress relaxation in the material. This is not accounted for so far and will be analyzed in future steps. The results should be considered as residual stress at the end of the production process.

As a next step, a 2D model of the full half of the two-dimensional cylindrical slice has to be considered. Thereby, the mutual influence of thick and thin side boundary value problem can be connected and its influence on the final stress distribution can be studied. Based thereon, an extension to a 3D model should be taken into account. In the future, the numerical simulation environment can be used to analyze the influence of process parameters and aim for targeted residual stress states which improve the final properties of the specimen, e.g., compressive stress at the surface. Therefore, the material parameters and microscopic constituents for changed processing as well as additional phases have to be provided, for which a full exploitation of time–temperature transformation diagrams based on the prevalent cooling rate is inevitable. The discussed simulations and experiments can be used for validation and calibration for the here presented numerical model.

Acknowledgements The authors thank the group of Prof. B.-A. Behrens from the Institute of Forming Technology and Machines, Leibniz University Hannover, for the provided data and scientific support.

Funding Open Access funding enabled and organized by Projekt DEAL. This work was funded by Deutsche Forschungsgemeinschaft (DFG, German Research Foundation) - 374871564 (BR 5278/3-2, SCHR 570/33-2) within the priority program SPP 2013.

Compliance with ethical standards

Conflict of interest On behalf of all authors, the corresponding author states that there is no conflict of interest.

References

1. Bain, E.C., Dunkirk, N.Y.: The nature of martensite. Trans. Am. Inst. Min. Metall. Eng. **70**, 25–47 (1924)
2. Bain, E.C., Griffiths, W.E.: An introduction to the iron-chromium-nickel alloys. Trans. Am. Inst. Min. Metall. Eng. **75**, 166–211 (1927)
3. Behrens, B.-A., Bouguecha, A., Götze, T., Moritz, J., Sunderkötter, C., Helmholz, R., Schrödter, J.: Numerical and experimental analysis of the phase transformation during a hot stamping process in consideration of strain-dependent CCT-diagrams. In: 4th International Conference Hot Sheet Metal Forming of High-Performance Steel CHS2, Lulea, pp. 329–336 (2013)
4. Behrens, B.-A., Schröder, J., Brands, D., Scheunemann, L., Niekamp, R., Sarhil, M., Uebing, S., Kock, C.: Experimental and numerical investigations on the development of residual stresses in thermo-mechanically processed Cr-alloyed steel 1.3505. Metals **9**(4), 480 (2019)
5. Bhattacharya, K.: Microstructure of Martensite, Why it Forms and How it Gives Rise to the Shape-Memory Effect. Oxford University Press, Oxford (2003)
6. Bonn, R.: *Experimentelle und numerische Ermittlung der thermo-mechanischen Beanspruchung des Wurzelbereichs austenitischer Rundstähle*. PhD thesis, Universität Stuttgart (2001)
7. Fei, D., Hodgson, P.: Experimental and numerical studies of springback in air v-bending process for cold rolled TRIP steels. Nucl. Eng. Des. **236**(18), 1847–1851 (2006)
8. Fischer, F.D., Berveiller, M., Tanaka, K., Oberaigner, E.R.: Continuum mechanical apsects of phase transformations in solids. Arch. Appl. Mech. **64**, 54–85 (1994)
9. Ganghoffer, J.F., Denis, S., Gautier, E., Simon, A., Simonsson, K., Sjöström, S.: Micromechanical simulation of a martensitic transformation by finite element. J. Phys. IV **1**(C4), C4–77 (1991)
10. JMatPro. Practical software for materials properties. August 2018. https://www.sentesoftware.co.uk/jmatpro
11. Levitas, V.I.: Condition of nucleation and interface propagation in thermoplastic materials. J. Phys. IV **5**, 41–46 (1995a)
12. Levitas, V.I.: Thermomechanics of martensitic phase transitions in elastoplastic materials. Mech. Res. Commun. **22**, 87–93 (1995b)
13. Levitas, V.I.: The postulate of realizability: formulation and applications to post-bifurcation behavior and phase transitions in elastoplastic materials. Part I and II. Int. J. Eng. Sci. **33**, 921–971 (1995c)
14. Levitas, V.I.: Phase transitions in inelastic materials at finite strains: a local description. J. Phys. IV **6**, 55–64 (1996)
15. Levitas, V.I.: Phase transitions in elastoplastic materials: continuum thermomechanical theory and examples of control. Part I. J. Mech. Phys. Solids **45**, 1203–1222 (1997a)

16. Levitas, V.I.: Phase transitions in elastoplastic materials: continuum thermomechanical theory and examples of control. Part II. J. Mech. Phys. Solids **45**, 923–947 (1997b)
17. Levitas, V.I.: Thermomechanical theory of martensitic phase transformation in inelastic materials. Int. J. Solids Struct. **45**, 923–947 (1998)
18. Levitas, V.I., Idesmann, A.V., Leshchuk, A.A., Polotnyak, S.B.: Numerical modeling of thermomechanical processes in high pressure apparatus applied for superhard materials synthesis. High Press. Sci. Technol. **4**, 38–40 (1989)
19. Levitas, V.I., Idesman, A.V., Stein, E.: Finite element simulation of martensitic phase transitions in elastoplastic materials. Int. J. Solids Struct. **35**, 855–887 (1998)
20. Ma, Y., Zhang, Y., Zhang, H., Xue, C.: Residual stress analysis of the multi-stage forging process of a nickel-based superalloy turbine disc. Proc. Inst. Mech. Eng. G J. Aerosp. Eng. **227**(2), 213–225 (2013)
21. Macherauch, E., Wohlfahrt, H., Wolfstied, U.: Härterei-Technische Mitteilungen - Zeitschrift für Werkstoffe. Wärmebehandlung Fert. **28**(3), 201–211 (1973)
22. Mahnken, R., Schneidt, A., Antretter, T.: Macro modelling and homogenization for transformation induced plasticity of a low-alloy steel. Int. J. Plast. **25**(2), 183–204 (2009)
23. McMeeking, R.M., Lee, E.H.: Residual Stress and Stress Relaxation: The Generation of Residual Stresses in Metal-Forming Processes, Chapter 17, pp. 315–329. Springer, Berlin (1982)
24. Miehe, C.: Zur numerischen behandlung thermomechanischer Prozesse. PhD thesis, Universität Hannover (1988)
25. Miehe, C., Schotte, J., Schröder, J.: Computational micro-macro transitions and overall moduli in the analysis of polycrystals at large strains. Comput. Mater. Sci. **16**(1–4), 372–382 (1999a)
26. Miehe, C., Schröder, J., Schotte, J.: Computational homogenization analysis in finite plasticity. Simulation of texture development in polycrystalline materials. Comput. Methods Appl. Mech. Eng. **171**(3–4), 387–418 (1999b)
27. Moen, C.D., Igusa, T., Schafer, B.W.: Prediction of residual stresses and strains in cold-formed steel members. Thin-Walled Struct. **46**(11), 1277–1289 (2008)
28. Moyer, J.M., Ansell, G.S.: The volume expansion accompanying the martensite transformation in iron-carbon alloys. Metall. Trans. A **6**(9), 1785–1791 (1975)
29. Müller, R.: A Phase Field Model for the Evolution of Martensitic Microstructures in Metastable Austenite. PhD thesis, Technische Universität Kaiserslautern (2016)
30. Mungi, M.P., Rasane, S.D., Dixit, P.M.: Residual stresses in cold axisymmetric forging. J. Mater. Process. Technol. **142**(1), 256–266 (2003)
31. Olle, P.: Numerische und experimentelle Untersuchungen zum Presshärten. PhD thesis, Fakultät für Maschinenbau, Gottfried Wilhelm Leibniz Universität Hannover (2010)
32. Olson, G.B., Cohen, M.: A mechanism for the strain-induced nucleation of martensitic transformations. J. Less-Common Met. **28**, 107–118 (1972)
33. Olson, G.B., Cohen, M.: A general mechanism of martensitic nucleation: part II FCC to BCC and other martensitic transformations. Metall. Trans. A **74**, 1905–1914 (1976)
34. Park, S.H.: Microstructural evolution of hot rolled TRIP steels during cooling control. In: 40th Mechanical Working and Steel Processing Conference. ISS/AIME, pp. 283–291, Pittsburgh (1998)
35. Roters, F., Eisenlohr, P., Hantcherli, L., Tjahjanto, D.D., Bieler, T.R., Raabe, D.: Overview of constitutive laws, kinematics, homogenization and multiscale methods in crystal plasticity finite-element modeling: theory, experiments, applications. Acta Mater. **58**, 152–1211 (2010)
36. Schneider, D., Schmid, S., Selzer, M., Böhlke, T., Nestler, B.: Small strain elasto-plastic multiphase-field model. Comput. Mech. **55**, 27–35 (2015)
37. Schneider, D., Schwab, F., Schoof, E., Reiter, A., Herrmann, C., Selzer, M., Böhlke, T., Nestler, B.: On the stress calculation within phase-field approaches: a model for finite deformations. Comput. Mech. **60**, 203–217 (2017)
38. Schoff, E., Schneider, D., Streichhan, N., Mittnacht, T., Selzer, M., Nestler, B.: Multiphase-field modeling of martensitic phase transformation in a dual-phase microstructure. Int. J. Solids Struct. **134**, 181–194 (2017)
39. Schröder, J.: A numerical two-scale homogenization scheme: the FE^2-method. In: Schröder, J., Hackl, K. (eds.) Plasticity and Beyond-Microstructures, Crystal-Plasticity and Phase Transitions, Volume 550 of CISM Courses and Lectures, pp. 1–64. Springer (2014)
40. Simo, J.C., Hughes, T.J.R.: Computational Inelasticity. Springer, Berlin (1998)
41. Simo, J.C., Miehe, C.: Associative coupled thermoplasticity at finite strains: formulation, numerical analysis and implementation. Comput. Methods Appl. Mech. Eng. **98**(1), 41–104 (1992)
42. Simonsson, K.: Micromechanical FE-Simulations of the Plastic Behavior of Steels Undergoing Martensitic Transformation. PhD thesis, Linköping University (1994)
43. Simsir, C., Gür, C.H.: 3D FEM simulation of steel quenching and investigation of the effect of asymmetric geometry on residual stress distribution. J. Mater. Process. Technol. **207**, 211–221 (2008)
44. Stringfellow, R.G., Parks, D.M., Olson, G.B.: A constitutive model for transformation plasticity accompanying strain-induced martensitic transformations in metastable austenitic steels. Acta Metall. Mater. **40**, 1703–1716 (1992)
45. Tekkaya, A.E., Gerhardt, J., Burgdorf, M.: Residual stresses in cold-formed workpieces. Manuf. Technol. **34**, 225–230 (1985)